

THE DIAGNOSTIC POTENTIAL OF Fe LINES APPLIED TO PROTOSTELLAR JETS*

T. GIANNINI¹, B. NISINI¹, S. ANTONIUCCI¹, J. M. ALCALÁ², F. BACCIOTTI³, R. BONITO^{4,5},
 L. PODIO⁶, B. STELZER⁴, AND E. T. WHELAN⁷

¹ INAF-Osservatorio Astronomico di Roma, via Frascati 33, I-00040 Monte Porzio Catone, Italy

² INAF-Osservatorio Astronomico di Capodimonte, via Moiariello 16, I-80131 Napoli, Italy

³ INAF-Osservatorio Astrofisico di Arcetri, Largo E. Fermi 5, I-50125 Firenze, Italy

⁴ INAF-Osservatorio Astronomico di Palermo, Piazza del Parlamento 1, I-90134 Palermo, Italy

⁵ Dipartimento di Fisica e Chimica, Università di Palermo, Piazza del Parlamento 1, I-90134 Palermo, Italy

⁶ UJF-Grenoble 1/CNRS-INSU, Institut de Planetologie et d'Astrophysique de Grenoble (IPAG) UMR 5274, Grenoble, F-38041, France

⁷ Institut für Astronomie und Astrophysik, Kepler Center for Astro and Particle Physics, Eberhard Karls Universität, D-72076 Tübingen, Germany

Received 2013 August 6; accepted 2013 September 19; published 2013 November 6

ABSTRACT

We investigate the diagnostic capabilities of iron lines for tracing the physical conditions of shock-excited gas in jets driven by pre-main sequence stars. We have analyzed the 3000–25000 Å, X-shooter spectra of two jets driven by the pre-main sequence stars ESO-Hα 574 and Par-Lup 3-4. Both spectra are very rich in [Fe II] lines over the whole spectral range; in addition, lines from [Fe III] are detected in the ESO-Hα 574 spectrum. Non-local thermal equilibrium codes solving the equations of the statistical equilibrium along with codes for the ionization equilibrium are used to derive the gas excitation conditions of electron temperature and density and fractional ionization. An estimate of the iron gas-phase abundance is provided by comparing the iron lines emissivity with that of neutral oxygen at 6300 Å. The [Fe II] line analysis indicates that the jet driven by ESO-Hα 574 is, on average, colder ($T_e \sim 9000$ K), less dense ($n_e \sim 2 \times 10^4 \text{ cm}^{-3}$), and more ionized ($x_e \sim 0.7$) than the Par-Lup 3-4 jet ($T_e \sim 13,000$ K, $n_e \sim 6 \times 10^4 \text{ cm}^{-3}$, $x_e < 0.4$), even if the existence of a higher density component ($n_e \sim 2 \times 10^5 \text{ cm}^{-3}$) is probed by the [Fe III] and [Fe II] ultra-violet lines. The physical conditions derived from the iron lines are compared with shock models suggesting that the shock at work in ESO-Hα 574 is faster and likely more energetic than the Par-Lup 3-4 shock. This latter feature is confirmed by the high percentage of gas-phase iron measured in ESO-Hα 574 (50%–60% of its solar abundance in comparison with less than 30% in Par-Lup 3-4), which testifies that the ESO-Hα 574 shock is powerful enough to partially destroy the dust present inside the jet. This work demonstrates that a multiline Fe analysis can be effectively used to probe the excitation and ionization conditions of the gas in a jet without any assumption on ionic abundances. The main limitation on the diagnostics resides in the large uncertainties of the atomic data, which, however, can be overcome through a statistical approach involving many lines.

Key words: ISM: individual objects (ESO-Hα 574, Par-Lup 3-4) – ISM: jets and outflows – ISM: lines and bands – stars: pre-main sequence

Online-only material: color figures

1. INTRODUCTION

Jets from young stars play a key role in the dynamics of star formation and disk evolution. They regulate the process of stellar accretion, by both removing the angular momentum generated by accreting material in the disk, and modifying the inner disk physics, thus influencing the evolution of proto-planetary systems. The specific role of jets in the dynamics and evolution of the accreting system strongly depends on the parameters that characterize their structure and excitation, which are in turn related to their formation and heating mechanisms. From an observational point of view, information on the jet physics and dynamics can be retrieved through the analysis of the forbidden lines emitted by the jet plasma when it gets excited in shocks: to this aim, strong optical lines, such as [O I], [S II], and [N II] lines, are widely used and specific diagnostic tools, able to retrieve a complete set of parameters (namely electron density, n_e , temperature, T_e , and ionization fraction, x_e), have been developed (e.g., Bacciotti & Eisloffel 1999). The knowledge of these parameters is fundamental to an understanding of jet

acceleration mechanisms (e.g., MHD disk-winds or X-winds; Shu et al. 1994; Ferreira 1997) and for measuring the mass flux rate (\dot{M}_{jet}). \dot{M}_{jet} is the quantity regulating the efficiency of the jet and is directly related to the disk mass accretion rate (\dot{M}_{acc}).

Although widely exploited and constantly refined, the diagnostic tools based on bright optical lines suffer from several intrinsic limitations. First, optical lines trace specific excitation conditions and hence force the assumption that the gas in the jet has a constant temperature and density. This assumption is in contrast with combined optical/near infrared line analysis, which has shown that gradients in temperature and density up to more than one order of magnitude usually occur in the cooling region behind the shock front (Nisini et al. 2005; Podio et al. 2006). Second, diagnostic tools based on ratios between lines of different atomic species require one to assume a set of elemental abundances, which in turn imply an uncertainty on the parameters (temperature and density) more than 40% (Podio et al. 2006). Finally, the use of optical lines requires an *a priori* knowledge of the visual extinction, a circumstance that often makes the optical diagnostic applicable only to jets of the more evolved sources, where the reddening is negligible. All the above limitations can be circumvented by using different lines of the same species, covering a wide range of wavelengths

* Based on observations collected with X-shooter at the Very Large Telescope on Cerro Paranal (Chile), operated by the European Southern Observatory (ESO). Program ID: 085.C-0238(A).

particularly sensitive to extinction variations. In this respect a diagnostic of iron (in different ionization stages) represents a very well suited tool. Indeed, since the iron line spectrum covers all the wavelengths between the ultraviolet (UV) and the near-infrared (NIR), it is sensitive to a large range of excitation conditions, which allows complete view of the post-shock cooling region to be derived. The aim of the present paper is to examine the potential of the iron lines in probing the jet physical parameters. Our test cases are two jets that we have observed with the X-shooter spectrograph in the wavelength range $\sim 3000\text{--}25000\text{ \AA}$, namely the jets excited by the sources ESO-H α 574 and Par-Lup 3-4.

ESO-H α 574 ($\alpha_{J2000.0} = 11^{\text{h}}16^{\text{m}}03^{\text{s}}.7$, $\delta_{J2000.0} = -76^{\circ}24'53''$), spectral type K8, is a low-luminosity source in the Chamaleon I star-forming region located at a distance $d = 160 \pm 17$ pc (Wichmann et al. 1998). The low luminosity of $3.4 \times 10^{-3} L_{\odot}$ (Luhman 2007), which is a factor ~ 150 lower than the luminosity of the typical T Tauri stars of the same spectral type, is interpreted as resulting from a disk seen edge-on. The source powers a bipolar jet (HH 872) of total projected length of 0.015 pc (3140 AU). It was discovered by Comerón & Reipurth (2006) in a [S II] image at 6728 \AA as a chain of knots, of which knots A1, A, B, C, D form the blue-shifted jet and knot E forms the red-shifted jet.

Par-Lup 3-4 ($\alpha_{J2000.0} = 16^{\text{h}}08^{\text{m}}51^{\text{s}}.44$, $\delta_{J2000.0} = -39^{\circ}05'30''$), spectral type M5, is located in the Lupus III dark cloud at $d = 200 \pm 40$ pc (Comerón et al. 2003). This object also appears to be under-luminous, being about 25 times fainter than typical M5 pre-main sequence objects ($L = 3 \times 10^{-3} L_{\odot}$; Merín et al. 2008). As in the case of ESO-H α 574, its low luminosity is likely due to the obscuration of the star by an edge-on viewing disk (Huélamo et al. 2010). The jet was discovered by Fernández & Comerón (2005), with emission extending in opposite directions with respect to the star for a total length of ~ 1240 AU.

The X-shooter spectra of the two objects have already been investigated by Bacciotti et al. (2011, hereinafter BWA11) and by Whelan et al. (2013, hereinafter WBA13). Both papers determine the mass ejection to mass accretion ratio $\dot{M}_{\text{jet}}/\dot{M}_{\text{acc}}$. While in Par-Lup 3-4 this ratio is at the upper end of the range predicted by jet models, the value found in ESO-H α 574 of ~ 90 can be partially reconciled with the predictions of magneto-centrifugal jet acceleration mechanisms only if the edge-on disk severely reduces the luminosity of the accretion tracers. The numerous spectral lines detected in the two jets, along with the kinematical properties derived in the line profiles are presented in WBA13.

In the present paper, we concentrate our analysis on the many iron lines detected in both spectra. The paper is outlined as follows. In Section 2 we briefly summarize the details of the observations and present the spectroscopic data; in Section 3 we describe the iron excitation and ionization models and derive the jet physical parameters. In Section 4 we discuss the results, which are summarized in Section 5.

2. OBSERVATIONS AND DATA

The present work is part of a series of papers that deal with our X-shooter survey of pre-main sequence objects. The overall aspects, such as scopes, data reduction procedures, calibrations, and results are thoroughly discussed in Alcalá et al. (2011) and Alcalá et al. (2013). Here we just recall the information that is essential for the presented subject. The X-shooter spectra of ESO-H α 574 and Par-Lup 3-4 were acquired on 2010

April 7, with an integration time of ~ 1 hr per object. The slit, aligned with the jet axis, was set to achieve a resolving power of 5100, 8800, and 5600 for the UVB (3000–5900 Å), VIS (5450–10200 Å), and NIR arm (9900–24700 Å), respectively (slit widths: 1'0, 0'9, 0'9). The pixel scale was 0'16 for the UVB and VIS arms and 0'21 for the NIR arm.

The data reduction was performed independently for each arm using the X-shooter pipeline version 1.1., which provides two-dimensional spectra, background-subtracted and calibrated in wavelength. Post-pipeline procedures were then applied by using routines within the IRAF and MIDAS packages to subtract sky lines and obtain one-dimensional spectra. These are then divided by a telluric spectrum to remove the atmospheric features, and to do the flux-calibration. The complete spectrum was obtained by comparing the flux densities in the overlapping portions of the spectra of adjacent arms. While UVB and VIS spectra are perfectly aligned, the NIR spectrum of ESO-H α 574 appears lower by a factor ~ 1.26 . Flux losses in the NIR arm are not uncommon in the X-Shooter spectra and are caused by a misalignment between the NIR with respect to the VIS and UVB arms (Alcalá et al. 2013). No correction was necessary to re-align the three arms spectra of Par-Lup 3-4.

As far as the ESO-H α 574 jet is concerned (hereinafter ESO-H α 574), we concentrate here on the iron lines detected in the brightest knot, A1. This is also the closest to the exciting source, extending from the source itself up to $2''$ away (320 AU; see Figure 2 of BWA11, upper panel). The Par-Lup 3-4 jet (hereinafter Par-Lup 3-4) was integrated up to a distance of $1''$ from the source continuum, which corresponds to 200 AU (see Figure 2 of BWA11, lower panel).

Figures 1 and 2 show the portions of the spectra of the two objects where iron lines are detected, while Figure 3 shows the Grotrian diagram of Fe $^{+}$ levels from which the detected lines originate. The maximum energy level is at more than $30,000\text{ cm}^{-1}$ above the ground state, and the line wavelengths cover the whole investigated range (in blue, green, and red we indicate ultra-violet, optical, and near-infrared lines, respectively). Similarly, Figure 4 gives the diagram of Fe $^{++}$ levels. Note that, due to the level structure, all the emitted lines lie only in the ultra-violet range, although the covered energy range is comparable to that of Fe $^{+}$.

The line fluxes of all the detected lines are listed in Table A.1 of WBA13. Here we give, in Table 1, the observed line ratios $R_{\text{ESO-H}\alpha\text{ 574}}$ and $R_{\text{Par-Lup 3-4}}$ of the [Fe II] lines detected in the two objects with respect to the bright line at 4277 \AA . Lines originating from the same multiplet are grouped together and listed in order of decreasing energy of the upper level. In the last column, the ratio $R_{\text{ESO-H}\alpha\text{ 574}}/R_{\text{Par-Lup 3-4}}$ is reported. Because the differential extinction between the two objects is negligible (see Section 3.1.1), this ratio gives a qualitative indication of whether or not the excitation conditions are similar in the two objects. Indeed, lines with excitation energy $\gtrsim 20,000\text{ cm}^{-1}$ (ultra-violet and optical lines) and those with excitation energy $\lesssim 20,000\text{ cm}^{-1}$ (near-infrared lines) have $< R_{\text{ESO-H}\alpha\text{ 574}}/R_{\text{Par-Lup 3-4}} > \approx 1.15$ and $< R_{\text{ESO-H}\alpha\text{ 574}}/R_{\text{Par-Lup 3-4}} > \approx 2.6$, respectively. This in practice suggests that in Par-Lup 3-4 the most excited lines are brighter (in comparison to the 4277 \AA) than in ESO-H α 574, a circumstance that could reflect a higher gas temperature.

Notably, [Fe III] lines are detected only in ESO-H α 574 (see Table 2). This result cannot be explained with a different sensitivity in the X-shooter spectra of the two jets, which are similarly bright and were integrated for a comparable amount of

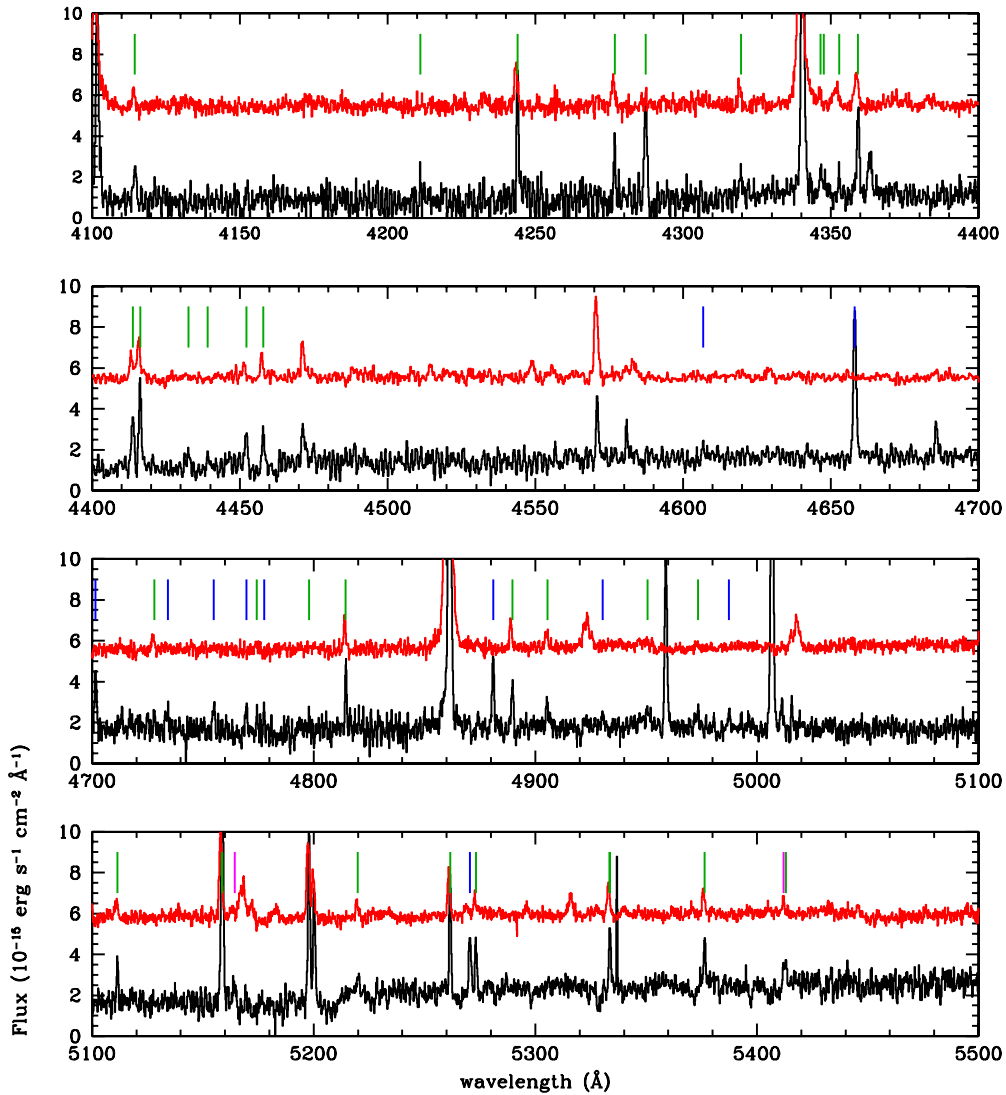


Figure 1. UVB spectrum of ESO-H α 574 (black) and Par-Lup 3.4 (red) where iron lines are detected. Green labels: [Fe II] lines; blue labels: [Fe III] lines; magenta labels: blends. For clarity, the spectrum of Par-Lup 3-4 was augmented by a factor of five (in the reported units).

(A color version of this figure is available in the online journal.)

time. Therefore, this feature also points to different excitation conditions in the two objects.

3. LINE FITTING MODEL

In this section we describe the excitation and ionization models that provide the main physical parameters of the two investigated jets. The results of the comparison between observations and models are summarized in Table 4.

3.1. The Excitation Model

The observed ratios between lines from the same ionic species (e.g., Fe⁺ or Fe⁺⁺) can be compared with the predictions by an excitation model to derive the physical conditions of the gas. To this aim we adopted a non-local thermal equilibrium (NLTE) approximation for line excitation. One of the main issues of such line modeling regards the choice of the atomic dataset. The complexity of the iron atomic system, which involves hundreds of energy levels (with multiple metastable levels), makes it very difficult to get accurate atomic data sets (both radiative and collisional). For example, seven different computations

of the Einstein coefficients for the spontaneous radiative decay (A-values) have been implemented for Fe⁺, which may differ from each other by more than 50%. Bautista et al. (2013) have evaluated the uncertainties in the line emissivities due to the combinations of the uncertainties on A-values, collisional coefficients, and propagation of these two on the level populations. For typical shock-excitation conditions, namely $T_e \sim 10,000$ K and density between 10^2 and 10^8 cm⁻³, they find a very wide range of uncertainties, which vary from less than 10% (e.g., lines at $1.256 \mu\text{m}$ and 8616 \AA) to more than 60% (e.g., lines at $5.330 \mu\text{m}$ and at 5527 \AA). As shown by the same authors, the most effective way to circumvent the problem is to apply a statistical approach by including a large number of lines in the analysis.

In our model we use the up-to-date atomic database of the XSTAR compilation (Bautista & Kallman 2001),⁸ which gives energy levels, A-values, and rates for collisions with electrons (these latter for temperatures between 2000 K and 20,000 K) for the first 159 and 34 fine-structure levels of Fe⁺ and Fe⁺⁺,

⁸ Available at heasarc.gsfc.nasa.gov/xstar/xstar.html.

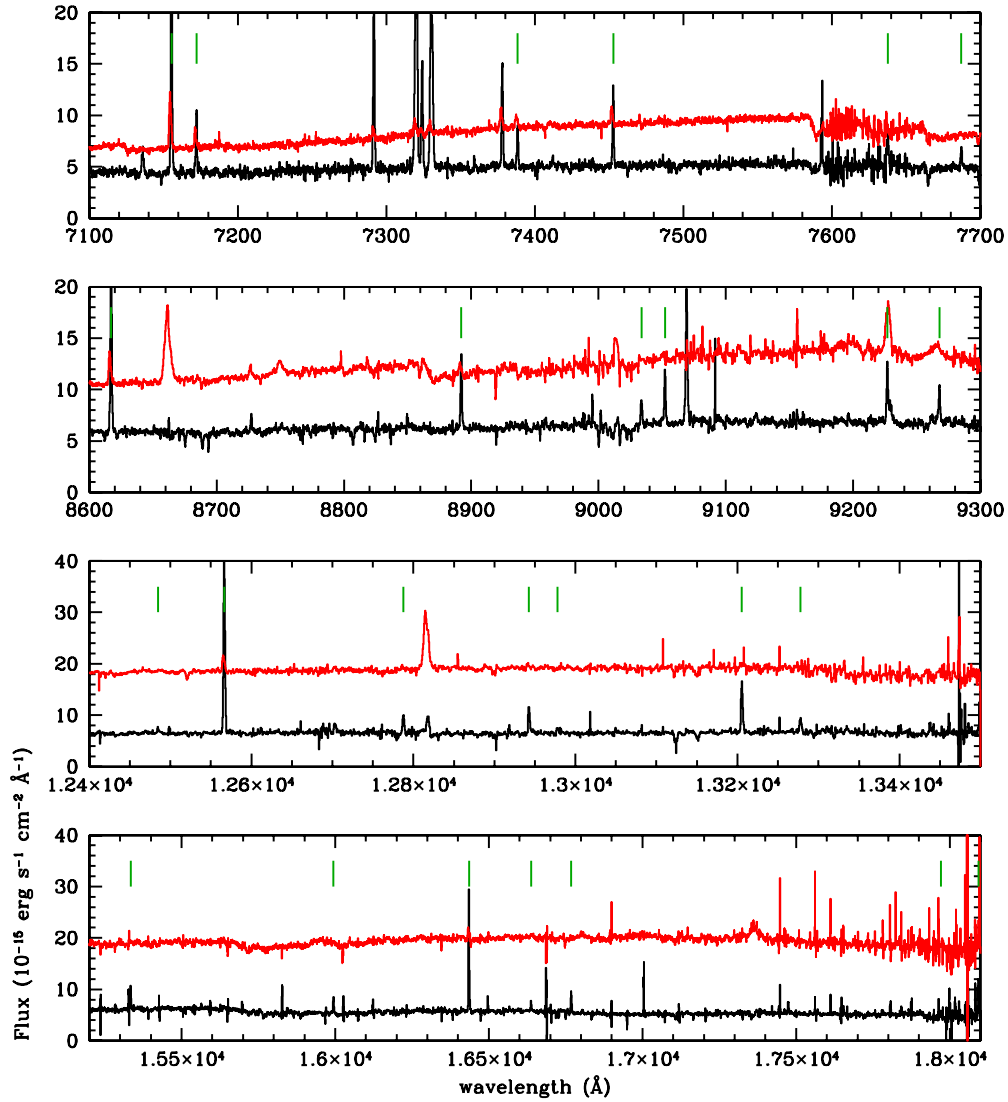


Figure 2. As in Figure 1 for the VIS and NIR spectra.
(A color version of this figure is available in the online journal.)

respectively. The implications on the results when adopting different data sets will be commented on in Section 3.1.1.

The NLTE model assumes electronic collisional excitation/de-excitation and spontaneous radiative decay. Possible contributions to line emissivities due to radiative processes are discarded at this step of the analysis, but will be considered in Section 3.3. The free parameters of the excitation model are the electron temperature T_e and the density n_e , which can be derived from the observed flux ratios once line fluxes are corrected for the visual extinction (A_V) along the line of sight. This latter parameter is usually derived from the flux ratio of the lines emitted from the same upper level, this being independent from the level population and therefore a function only of the line frequencies and the A-coefficients. As stated above, however, the large uncertainties associated with these latter values, are reflected in a poor estimate of A_V , especially if one considers only two or three lines, as is often done with the NIR [Fe II] lines (see also Giannini et al. 2008). Therefore, we have taken the extinction as a further free parameter of the excitation model. To derive the differential extinction at each line wavelength, we adopt the extinction curve by Draine (2003). To minimize the uncertainties, we included in the fit only the un-blended lines

detected with a signal-to-noise ratio (S/N) larger than 5 (i.e., 35 lines for ESO-H α 574 and 20 lines for Par-Lup 3-4) and checked the compatibility of the fit with line fluxes at lower S/N a posteriori. First, we constructed a grid of model solutions in the parameter space $2000 \text{ K} < T_e < 30,000 \text{ K}$ (in steps of $\delta T_e = 1000 \text{ K}$); $10^2 \text{ cm}^{-3} < n_e < 10^7 \text{ cm}^{-3}$ (in steps of $\log_{10}(\delta n_e/\text{cm}^{-3}) = 0.1$); and $A_V \leq 2 \text{ mag}$ (in steps of $\delta A_V = 0.5 \text{ mag}$). Then, following the method for line fitting proposed by Hartigan & Morse (2007), we iteratively changed the line used for the normalization, hence considering all the possible sets of line ratios. Each set was then compared with the grid of theoretical values to find the model with the lowest value of χ^2 .

3.1.1. [Fe II] Lines Fit

The result of the excitation model considering the complete set of [Fe II] lines detected in ESO-H α 574 is depicted in Figure 5. The minimum χ^2 -value is found if the line at 4277 Å is taken as a reference and the corresponding line ratios are reported in Table 1. The best-fit of the ESO-H α 574 [Fe II] lines gives the following parameters: $A_V = 0 \text{ mag}$, $T_e = 9000 \text{ K}$, and $n_e = 2.0 \cdot 10^4 \text{ cm}^{-3}$. A gas component at a single pair (T_e, n_e) fits reasonably well all the lines, but systematically underestimates

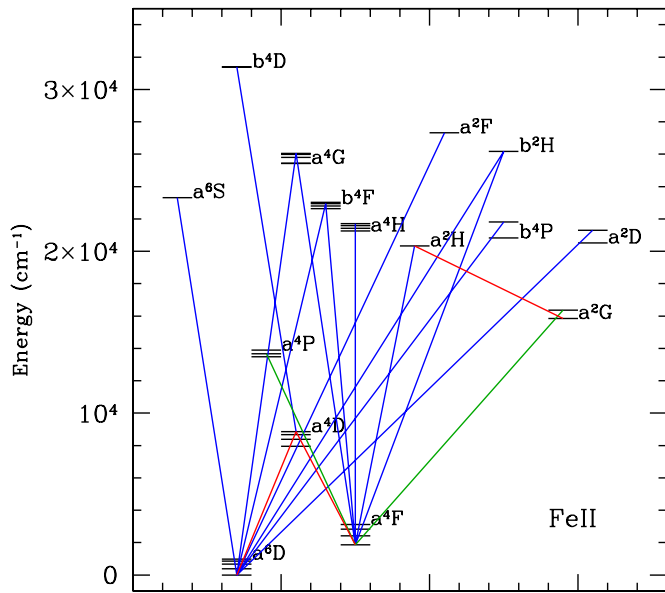


Figure 3. Grotrian diagram of Fe^+ levels associated with the observed lines. Groups of lines detected in different X-shooter arms are depicted with different colors: blue: ultra-violet lines; green: optical lines; red: near-infrared lines.

(A color version of this figure is available in the online journal.)

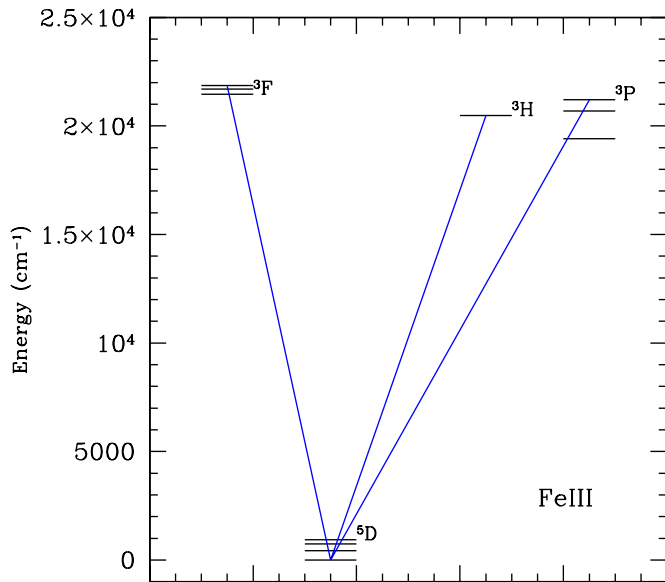


Figure 4. As in Figure 3 for the Fe^{++} levels.

(A color version of this figure is available in the online journal.)

those coming from some doublet and sextet levels (b^2H , a^6S , and a^2G), as shown with different colors in Figure 5 and reported in Table 3. In particular, ratios involving lines from a^6S and a^2G levels (eight lines) are underestimated by a factor of two, while those from level b^2H (two lines) are underestimated by a factor of four. This systematic behavior, which can be reasonably ascribed to the poor knowledge of the atomic parameters, has been already evidenced by Bautista & Pradhan (1998) for the a^6S level. Notably, however, the same model is selected as best-fit irrespective from including or not the doublets and sextets in the fit, although with a higher minimum reduced- χ^2 (hereinafter χ^2) in the latter case.

The sensitivity of the line ratios to the fitted parameters is probed in Figure 6, where we plot the χ^2 -contours in the

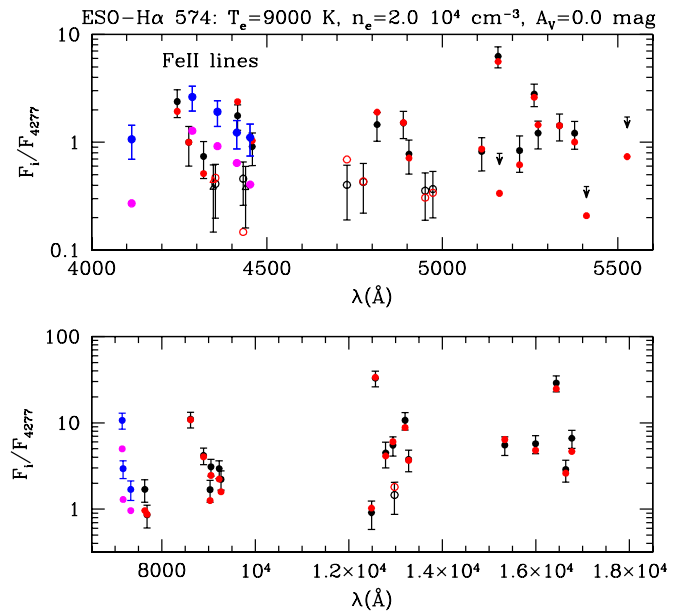


Figure 5. NLTE best-fit model of the $[\text{Fe II}]$ lines detected in ESO-H α 574. In the fitting procedure we have included the lines detected with $S/N \geq 5$, represented as filled circles (black: data; red: model). Lines detected with $3 \leq S/N < 5$ and $2 \leq S/N < 3$ are reported with open circles and open triangles, respectively. Down arrows are the fluxes of blended lines. Blue filled circles and magenta filled circles indicate the observed data and model predictions of lines coming from levels b^2H , a^6S , and a^2G , which are not included in the fitting procedure (see the text). The best-fit parameters are reported as well.

(A color version of this figure is available in the online journal.)

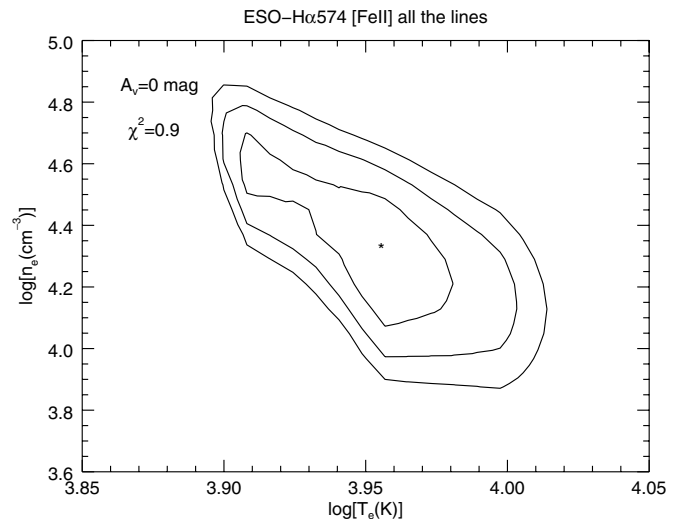


Figure 6. χ^2 -contours of the fit through the $[\text{Fe II}]$ lines detected in ESO-H α 574. The curves refer to increasing values of χ^2 of 30%, 60%, and 90%. The minimum χ^2 value is also given.

density-temperature plane for $A_V = 0$ mag (minimum $\chi^2 = 0.9$). Higher A_V values return fits with substantially higher χ^2 and are therefore discarded (for example minimum $\chi^2 = 1.9$ for $A_V = 0.5$ mag); this indicates that extinction decreases slightly from the ESO-H α 574 central source (where $A_V \sim 1.5$ mag, WBA13) to the jet. The plotted contours refer to increasing χ^2 values of 30%, 60%, and 90%, with respect to the minimum χ^2 value. From this plot we derive that temperature and density do not exceed (inside a confidence of 3σ) the ranges $8000 \text{ K} \lesssim T_e \lesssim 11,000 \text{ K}$ and $6 \times 10^3 \text{ cm}^{-3} \lesssim n_e \lesssim 6 \times 10^4 \text{ cm}^{-3}$, respectively.

Table 1
[Fe II] Lines

Line ID	λ_{air} (Å)	E_{up} (cm ⁻¹)	$(R \pm \Delta R)_{\text{ESO-H}\alpha\ 574}^*$	$(R \pm \Delta R)_{\text{Par-Lup 3-4}}^*$	R_E/R_P^*
b⁴D_{5/2}-a⁴D_{5/2}	4347.35	31387.9	0.4 ± 0.2**	<0.3	...
b⁴D_{1/2}-a⁴D_{1/2}	4438.91	31368.4	0.4 ± 0.2**	<0.3	...
a²F_{7/2}-a⁴D_{7/2}^a	5163.95	27314.9	0.8 ± 0.3	<0.3	...
b²H_{11/2}-a⁴F_{9/2}	4114.46	26170.2	1.1 ± 0.4	0.6 ± 0.3**	2.7
b²H_{11/2}-a⁴F_{7/2}	4211.09	26170.2	0.5 ± 0.2	<0.7	...
a⁴G_{7/2}-a⁴F_{5/2}	4319.61	25981.6	0.7 ± 0.3	0.7 ± 0.2	1.0
a⁴G_{9/2}-a⁴F_{5/2}	4352.77	25805.3	0.4 ± 0.2	0.5 ± 0.2	0.8
a⁴G_{11/2}-a⁴F_{9/2}	4243.96	25428.8	2.4 ± 0.7	1.8 ± 0.4	1.3
a⁴G_{11/2}-a⁴F_{7/2}	4346.85	25428.8	0.3 ± 0.2**	0.6 ± 0.2	0.5
a⁶S_{5/2}-a⁶D_{9/2}	4287.39	23317.6	2.6 ± 0.7	<0.4	...
a⁶S_{5/2}-a⁶D_{7/2}	4359.33	23317.6	1.9 ± 0.5	1.5 ± 0.3	1.3
a⁶S_{5/2}-a⁶D_{5/2}	4413.78	23317.6	1.2 ± 0.4	1.2 ± 0.2	1.0
a⁶S_{5/2}-a⁶D_{3/2}	4452.09	23317.6	1.1 ± 0.4	0.5 ± 0.2	2.2
b⁴F_{3/2}-a⁴F_{5/2}	4950.74	23031.3	0.4 ± 0.2	<0.2	...
b⁴F_{5/2}-a⁴F_{5/2}	4973.38	22939.4	0.4 ± 0.2	<0.3	...
b⁴F_{5/2}-a⁶D_{7/2}	4432.44	22939.4	0.5 ± 0.2	<0.3	...
b⁴F_{7/2}-a⁶D_{7/2}	4457.94	22810.4	0.9 ± 0.3	0.8 ± 0.2	1.1
b⁴F_{7/2}-a⁴F_{9/2}	4774.71	22810.4	0.4 ± 0.2	<0.2	...
b⁴F_{7/2}-a⁴F_{7/2}	4905.33	22810.4	0.8 ± 0.3	0.7 ± 0.2	1.1
b⁴F_{9/2}-a⁶D_{9/2}	4416.26	22637.2	1.8 ± 0.4	1.7 ± 0.3	1.0
b⁴F_{9/2}-a⁴F_{9/2}	4814.53	22637.2	1.5 ± 0.4	1.1 ± 0.2	1.4
a⁴H_{7/2}-a⁴F_{3/2}	5376.45	21711.9	1.2 ± 0.3	1.3 ± 0.3	0.9
a⁴H_{9/2}-a⁴F_{5/2}	5220.05	21581.6	0.8 ± 0.3	0.8 ± 0.2	1.0
a⁴H_{9/2}-a⁴F_{9/2}	5333.64	21581.6	1.4 ± 0.4	1.6 ± 0.3	0.9
a⁴H_{11/2}-a⁴F_{9/2}	5111.62	21430.4	0.8 ± 0.3	1.0 ± 0.2	0.8
a⁴H_{11/2}-a⁴F_{7/2}	5261.62	21430.4	2.8 ± 0.7	2.1 ± 0.3	1.3
a⁴H_{13/2}-a⁴F_{9/2}	5158.77	21251.6	6.3 ± 1.4	3.7 ± 0.6	1.7
b⁴P_{3/2}-a⁶D_{5/2}	4728.06	21812.1	0.4 ± 0.2	0.7 ± 0.2	0.6
b⁴P_{3/2}-a⁶D_{1/2}	4798.27	21812.1	0.3 ± 0.2**	<0.2	...
b⁴P_{5/2}-a⁶D_{7/2}	4889.61	20830.6	1.5 ± 0.4	0.9 ± 0.2	1.7
b⁴P_{5/2}-a⁴F_{9/2}	5273.34	20830.6	1.2 ± 0.3	0.9 ± 0.2	1.3
a²D_{3/2}-a⁴F_{5/2}^b	5412.65	21308.0	0.4 ± 0.2	0.4 ± 0.1	1.0
a²D_{5/2}-a⁴F_{7/2}^c	5527.33	20517.0	1.7 ± 0.5	1.9 ± 0.3	0.9
a²H_{11/2}-a⁴F_{9/2}	5413.34	20340.3	0.5 ± 0.2	<0.3	...
a²G_{7/2}-a⁴F_{7/2}	7172.00	16369.4	2.9 ± 0.7	1.6 ± 0.3	1.8
a²G_{7/2}-a⁴F_{5/2}	7388.17	16369.4	1.7 ± 0.4	1.7 ± 0.3	1.0
a²G_{9/2}-a⁴F_{9/2}	7155.16	15844.6	10.7 ± 2.2	5.4 ± 0.8	2.0
a²G_{9/2}-a⁴F_{7/2}	7452.54	15844.6	3.2 ± 0.7	1.9 ± 0.3	1.7
a⁴P_{1/2}-a⁴F_{5/2}	9033.49	13904.8	1.7 ± 0.5	<1.3	...
a⁴P_{1/2}-a⁴F_{3/2}	9267.56	13904.8	2.2 ± 0.5	<1.3	...
a⁴P_{5/2}-a⁶D_{5/2}	7637.50	13474.4	1.7 ± 0.4	0.8 ± 0.3	2.1
a⁴P_{5/2}-a⁴F_{9/2}	8616.95	13474.4	11.0 ± 2.2	3.8 ± 0.7	2.9
a⁴P_{5/2}-a⁴F_{7/2}	9051.94	13474.4	3.1 ± 0.7	<1.3	...
a⁴P_{3/2}-a⁶D_{5/2}	7686.93	13673.2	0.9 ± 0.3	<0.3	...
a⁴P_{3/2}-a⁶D_{7/2}	8891.91	13673.2	4.2 ± 0.9	1.7 ± 0.7	2.5
a⁴P_{3/2}-a⁶F_{5/2}^d	9226.61	13673.2	3.0 ± 0.7	11.9 ± 2.0	...
a⁴D_{1/2}-a⁴F_{5/2}	16637.6	8846.8	2.9 ± 0.8	<2.3	...
a⁴D_{3/2}-a⁴F_{3/2}	12787.7	8680.4	4.5 ± 1.5	2.1 ± 0.7	2.1
a⁴D_{3/2}-a⁴F_{1/2}	12977.7	8680.4	1.5 ± 0.6	<3.1	...
a⁴D_{3/2}-a⁴F_{7/2}	15994.7	8680.4	5.7 ± 1.3	<1.7	...
a⁴D_{3/2}-a⁴F_{5/2}	17971.0	8680.4	1.5 ± 0.7	<1.7	...
a⁴D_{5/2}-a⁶D_{7/2}	12485.4	8391.9	0.9 ± 0.3	<3.1	...
a⁴D_{5/2}-a⁶D_{5/2}	12942.6	8391.9	5.5 ± 1.4	1.9 ± 0.7	2.9
a⁴D_{5/2}-a⁶D_{3/2}	13277.7	8391.9	3.8 ± 1.0	<3.1	...
a⁴D_{5/2}-a⁶D_{9/2}	15334.7	8391.9	5.5 ± 1.3	<1.7	...
a⁴D_{5/2}-a⁶D_{7/2}	16768.7	8391.9	6.6 ± 1.5	<2.3	...
a⁴D_{7/2}-a⁶D_{9/2}	12566.8	7955.3	32.9 ± 6.8	7.4 ± 1.3	4.4
a⁴D_{7/2}-a⁶D_{7/2}	13205.5	7955.3	10.7 ± 2.4	<3.1	...
a⁴D_{7/2}-a⁴F_{9/2}	16435.4	7955.3	28.9 ± 6.0	6.3 ± 1.2	4.6
a⁴D_{7/2}-a⁴F_{7/2}	18093.9	7955.3	6.3 ± 2.0	<3.1	...

Notes. Bold values are used to easily identify groups of lines coming from the multiplet.

* $R_{\text{ESO-H}\alpha\ 574}$ and $R_{\text{Par-Lup 3-4}}$ are both computed with respect to the line $a^4G_{9/2}-a^4F_{7/2}$ at 4276.82 Å, whose flux is $(2.5 \pm 0.5) \times 10^{-17}$ erg s⁻¹ cm⁻² in ESO-Hα 574, knot A1, and $(1.7 \pm 0.2) \times 10^{-17}$ erg s⁻¹ cm⁻² in Par-Lup 3-4. R_E/R_P is the ratio $R_{\text{ESO-H}\alpha\ 574}/R_{\text{Par-Lup 3-4}}$.

**Line with signal-to-noise ratio between 2 and 3.

^a Blended with [Cr II] c²F_{7/2}-a⁴G_{9/2} at 5164.45 Å.

^b Blended with [Fe III] ³P₂-³D₁ at 5412.08 Å.

^c Blended with [Fe II] b²P_{1/2}-a⁴D_{1/2} at 5527.60 Å.

^d In Par-Lup 3-4 blended with He I ³P₀-³D₀.

Table 2
[Fe II] Lines in ESO-H α 574- knot A1

Line ID	λ_{air} (Å)	E_{up} (cm $^{-1}$)	$R \pm \Delta^* R$
$^3F_2 - ^5D_2$	4733.91	21857.2	0.8 ± 0.3
$^3F_2 - ^5D_1$	4777.68	21857.2	1.2 ± 0.5
$^3F_3 - ^5D_4$	4607.03	21699.9	1.3 ± 0.6
$^3F_3 - ^5D_3$	4701.53	21699.9	2.8 ± 0.7
$^3F_3 - ^5D_2$	4769.43	21699.9	1.4 ± 0.5
$^3F_4 - ^5D_4$	4658.05	21462.2	7.6 ± 1.6
$^3F_4 - ^5D_3$	4754.69	21462.2	1.8 ± 0.6
$^3H_4 - ^5D_4$	4881.00	20481.9	3.8 ± 1.0
$^3H_4 - ^5D_3$	4987.2	20481.9	1.1 ± 0.4
$^3P_1 - ^5D_2$	5011.25	20688.4	1.8 ± 0.6
$^3P_2 - ^5D_3$	5270.40	19404.8	3.3 ± 0.8
$^3P_2 - ^5D_1^a$	5411.98	19404.8	1.2 ± 0.6

Notes. Bold values are used to easily identify groups of lines coming from the multiplet.

* Te flux ratio R is computed with respect to the $^3F_2 - ^5D_2$ line at 4930.53 Å, whose flux is $(1.2 \pm 0.2) \times 10^{-17}$ erg s $^{-1}$ cm $^{-2}$.

^a Blended with [Fe II] $a^2D_{3/2} - a^4F_{5/2}$ at 5412.65 Å.

Table 3
[Fe II] Lines Coming from Doublet and Sextet Levels Underestimated by the NLTE Model

Line ID	λ_{air} (Å)
$b^2H_{11/2} - a^4F_{9/2}$	4114.46
$b^2H_{11/2} - a^4F_{7/2}$	4211.09
$a^6S_{5/2} - a^6D_{9/2}$	4287.39
$a^6S_{5/2} - a^6D_{7/2}$	4359.33
$a^6S_{5/2} - a^6D_{5/2}$	4413.78
$a^6S_{5/2} - a^6D_{3/2}$	4452.09
$a^2G_{7/2} - a^4F_{7/2}$	7172.00
$a^2G_{7/2} - a^4F_{5/2}$	7388.17
$a^2G_{9/2} - a^4F_{9/2}$	7155.16
$a^2G_{9/2} - a^4F_{7/2}$	7452.54

To check the reliability of the results, we have also attempted two different approaches: (1) to fit the data with a different set of collisional coefficients (Bautista & Pradhan 1998), which returns the same physical parameters but with a higher minimum χ^2 , and (2) to fit the ultra-violet component and the infrared components separately, with the aim of testing the possibility of the presence of different gas components. The χ^2 -contours of the ultra-violet lines fit (Figure 7) shows a best-fit value not significantly different from that obtained by the all-lines fit. Analogously, the temperature range does not significantly differ from that found in the all-lines fit. More interestingly, the density range traced by the ultra-violet lines points to higher densities (i.e., up to $10^{5.8}$ cm $^{-3}$ within a 3σ confidence level). This suggests that while temperature is fairly constant in the probed region (or that its variations occur over spatial scales much smaller than the angular resolution), density may be subjected to stronger gradients. Finally, the fit of the infrared lines (not shown here) gives results in good agreement with the all-lines fit.

In Figure 8 we show the best-fit model for the [Fe II] lines observed in Par-Lup 3-4. The minimum χ^2 is found, as in the case of ESO-H α 574, by taking as a reference the 4277 Å line. To better compare the line emission observed in this object with that of ESO-H α 574, we also plot, together with the line ratios of the detected lines, the 2σ upper limits at the wavelength

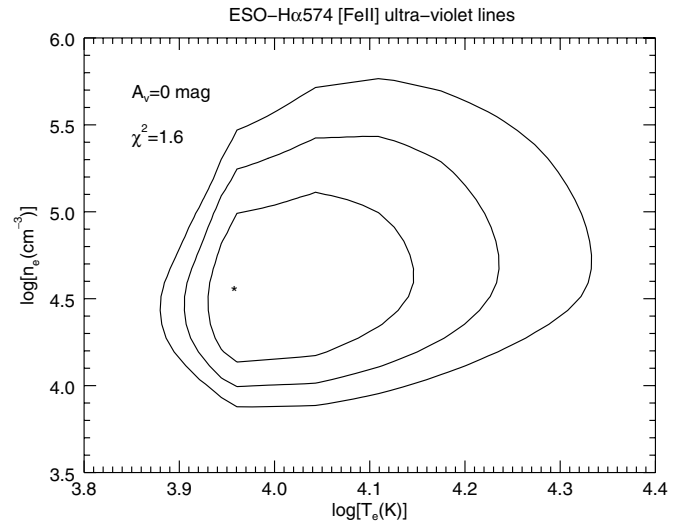


Figure 7. As in Figure 6 for the fit of the [Fe II] ultra-violet lines detected in ESO-H α 574.

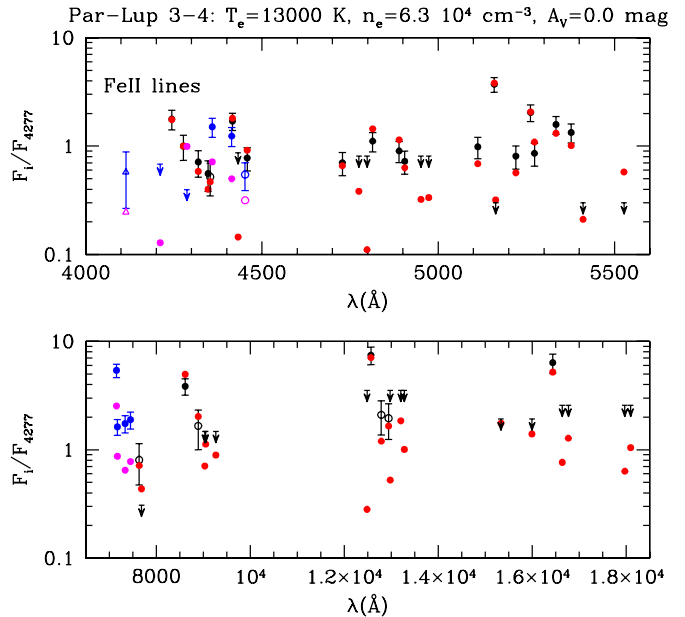


Figure 8. NLTE best-fit model of the [Fe II] lines detected in Par-Lup 3-4. In the fitting procedure the lines detected with $S/N \geq 5$, represented as filled circles (black: data; red: model) have been included. Lines detected with $3 \leq S/N < 5$ and $2 \leq S/N < 3$ are reported with open circles and open triangles, respectively. Down arrows are the blended lines or the 2σ upper limits of lines not detected in Par-Lup 3-4 but detected in ESO-H α 574. With blue and magenta symbols we indicate the observed data and model predictions of lines coming from levels b^2H , a^6S , and a^2G , which are not included in the fitting procedure. The best-fit parameters are also reported.

(A color version of this figure is available in the online journal.)

of the lines detected only in ESO-H α 574. As anticipated in Section 2, in Par-Lup 3-4 the ratios between ultra-violet and optical/near-infrared lines are substantially higher. This circumstance is a consequence of the higher temperature probed ($T_e = 13,000$ K). The inferred electron density and extinction are $n_e = 6.0 \times 10^4$ cm $^{-3}$ and $A_v = 0$ mag, respectively. As for ESO-H α 574, we find that the predictions of sextet and doublet levels are systematically underestimating the observed ratios of a factor between two and three. Within a confidence level of 90%, the χ^2 -contour plot gives $11,000 \text{ K} \lesssim T_e \lesssim 20,000 \text{ K}$ and $1.8 \times 10^4 \text{ cm}^{-3} \lesssim n_e \lesssim 1.8 \times 10^5 \text{ cm}^{-3}$ (see Figure 9). Finally, if the collisional coefficients by Bautista & Pradhan (1998) are

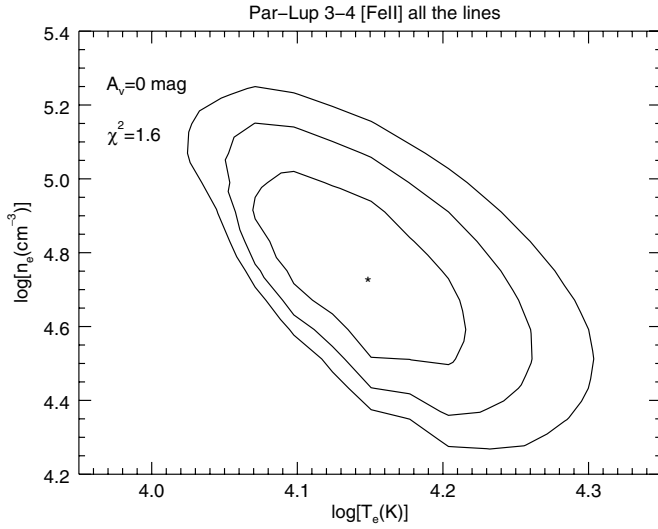


Figure 9. As in Figure 6 for the fit of the [Fe II] lines detected in Par-Lup 3-4.

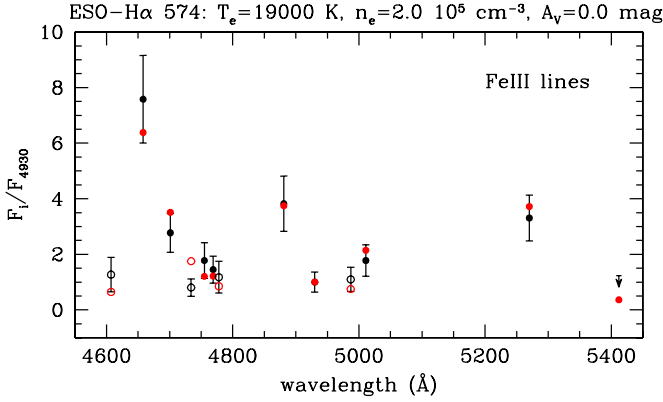


Figure 10. NLTE best-fit model of the [Fe III] lines detected in ESO-Halpha 574. The symbols have the same meaning as in Figure 5.

(A color version of this figure is available in the online journal.)

adopted, the best-fit gives $T_e = 16,000$ K, $n_e = 8.0 \times 10^4$ cm $^{-3}$, and $A_V = 0$ mag.

3.1.2. [Fe III] Lines Fit

The fit of [Fe III] lines detected in ESO-Halpha 574 is presented in Figure 10. The best-fit model is obtained by taking as a reference the line at 4930 Å (see also Table 2). This gives the following parameters: $T_e = 19,000$ K, $n_e = 2.0 \times 10^5$ cm $^{-3}$, and $A_V = 0$ mag. At variance with Fe $^{+}$ lines, all lines of Fe $^{++}$ lie in the ultra-violet range and come from levels with similar upper energy. Consequently, we expect that Fe $^{++}$ lines are poorly sensitive to the temperature. This is clear in the χ^2 -contour plot of Figure 11, where all the temperatures in the grid of NLTE solutions above 8000 K are compatible with the observations (within a confidence level of 90%). Conversely, the electron density is better constrained within the range 1×10^5 cm $^{-3} \lesssim n_e \lesssim 6 \times 10^5$ cm $^{-3}$. This result confirms that indeed a density gradient exists along the jet of ESO-Halpha 574, and that [Fe III] and [Fe II] ultra-violet lines likely probe the same, high-density gas component.

3.2. The Ionization Model

To consistently interpret the [Fe II] and [Fe III] emission in ESO-Halpha 574 and to derive the fractional abundance Fe $^{+}$ /Fe $^{++}$,

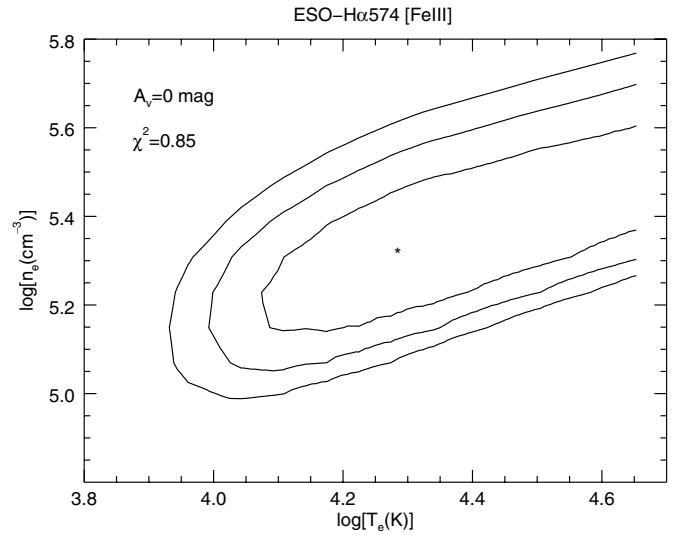


Figure 11. As in Figure 6 for the fit of the [Fe III] lines detected in ESO-Halpha 574.

we applied a ionization equilibrium code that involves the first four ionization stages of iron. The following processes have been taken into account: direct ionization, radiative and dielectronic recombination (data from Arnaud & Raymond 1992), and direct and inverse charge-exchange with hydrogen (data from Kingdon & Ferland 1996). Notably, while the first three processes are a function only of the electron temperature, direct and inverse charge-exchange rates also depend on the fractional ionization $x_e = n_e/n_H$, where $n_H = n_{H^0} + n_{H^+}$. Moreover, since the electron transfer is more efficient when the involved ions (e.g., H 0 and Fe $^{+}$) have similar ionization potentials (IP),⁹ the charge-exchange rate is relevant only for the process Fe $^{+} + H^0 \rightleftharpoons Fe^{++} + H^0$. Therefore, it returns relevant results for the Fe $^{+}$ /Fe $^{++}$ abundance ratio, while it is negligible for both the Fe 0 /Fe $^{+}$ and Fe $^{++}$ /Fe $^{+3}$ abundance ratios.

For $T_e = 8000$ K, which was the lowest temperature derived from the χ^2 -contours of Figures 6 and 7, our model predicts a substantial fraction of iron in neutral form even if the gas is almost fully ionized (e.g., we get 30% of Fe 0 , 52% of Fe $^{+}$, and 18% of Fe $^{++}$ for $x_e = 0.9$). This strongly contrasts with the simultaneous lack of any Fe 0 line in the ESO-Halpha 574 spectrum together with the presence of Fe $^{++}$ lines. However, just a slight increase of the electron temperature at 9000 K makes the neutral Fe 0 percentage drop to less than 10%, and that of Fe $^{++}$ to increase to more than 20%, in agreement with the observations. The expected percentage of Fe $^{+3}$ is negligible for the whole range of temperature considered in Figures 6 and 7.

To derive x_e we solved the ionization equilibrium equations (together with the excitation equilibrium for each of the two species) to predict a number of [Fe II]/[Fe III] line ratios. We constructed a grid of model solutions in the range $0 \leq x_e \leq 1$ (in steps of $\delta x_e = 0.05$) and $9000 \text{ K} \leq T_e \leq 14,000 \text{ K}$, being the upper value that was derived from the χ^2 -contours of Figure 7. To estimate x_e we consider the [Fe II] ultra-violet lines and the [Fe III] lines, assuming that they come from the same portion of the post-shock gas (see Section 3.1.2). We consider 14 line ratios involving 7 [Fe II] lines with 2 bright [Fe III] lines at 4701.59 Å and 5270.53 Å. As an example, we show in the upper panel of Figure 12, the [Fe II] 4244/[Fe III] 5270 ratio as a function of x_e

⁹ Being IP (Fe 0) = 7.87 eV, IP (Fe $^{+}$) = 16.18 eV, and IP (Fe $^{++}$) = 30.64 eV, to be compared with IP(H 0) = 13.595 eV.

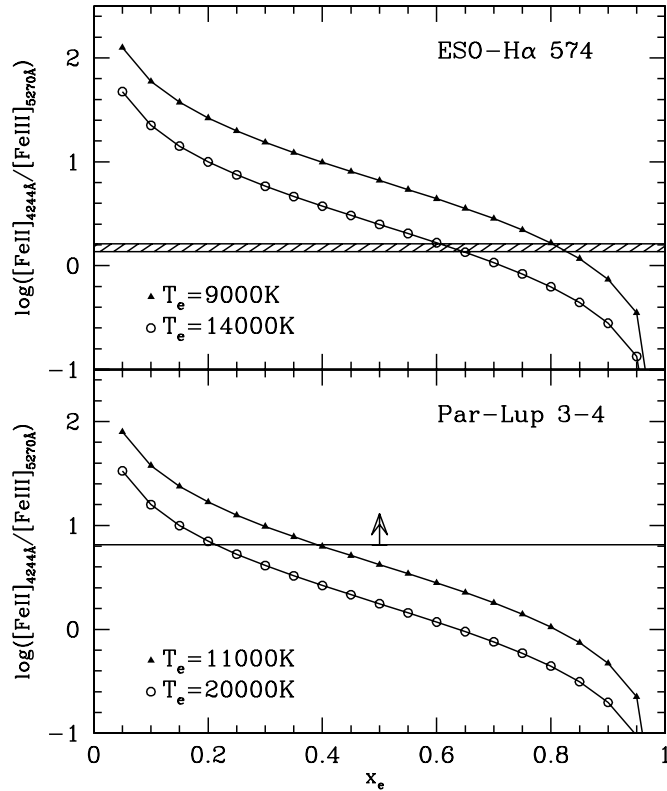


Figure 12. $[\text{Fe II}] 4244 \text{ \AA} / [\text{Fe III}] 5270 \text{ \AA}$ line ratio as a function of the fractional ionization for different values of the electron temperature. The ratio measured in ESO-H α 574 (upper panel) and Par-Lup 3-4 (lower panel) is depicted with an horizontal line.

for the considered range of temperature. The observations are in agreement with $0.65 \lesssim x_e \lesssim 0.85$, where the lower (upper) value refers to the highest (lowest) temperature assumed. This value of x_e is the same found (within the error range) if all the 14 ratios are considered.

For Par-Lup 3-4 we can derive an upper limit on x_e by considering the upper limits on the $[\text{Fe III}]$ lines. Taking a grid in the range $11,000 < T_e < 20,000 \text{ K}$ (see Section 3.1.1 and Figure 9), we get $x_e \lesssim 0.4$. As an example, the derivation of x_e from the ratio $[\text{Fe II}] 4244 / [\text{Fe III}] 5270$ is shown in the lower panel of Figure 12.

Typical x_e values in protostellar jets range from 0.03 to 0.6 (Ray et al. 2007; Nisini et al. 2005; Podio et al. 2009), although $x_e = 0.8$ is found in the High Velocity Component (HVC) of the DG Tau B jet (Podio et al. 2011). Therefore, while the fractional ionization of Par-Lup 3-4 is in the range of the most common values, that of ESO-H α 574 appears remarkably high.

3.3. Photoexcitation Contribution

In Section 3.1.1. the observed line ratios were interpreted in the light of collisional excitation. In this section we explore whether an additional contribution from fluorescence excitation is relevant. In ESO-H α 574 this possibility is supported by the detection of bright $[\text{Ni II}]$ lines at 7377.8 \AA and 7411.6 \AA (WBA13), whose intensity is easily enhanced because of the pumping of an ultra-violet field (Lucy 1995), although the observed intensity ratio of around 10 is compatible only with collisional excitation (see Figure 2 of Bautista et al. 1996). In Par-Lup 3-4, only the 7377.8 \AA line is detected.

To better investigate the role of photo-excitation in ESO-H α 574, we have included in the excitation model a radiation field,

which can be produced either from the stellar photosphere or by a hot spot on the stellar surface produced by the accretion shock of the infalling matter. Both these fields have been approximated as $W \times B_\nu(T_{\text{eff}})$, where B_ν is the blackbody function at the stellar (or hot spot) temperature and $W = 1/4 (R/r)^2$ is the dilution factor, having adopted the stellar radius $R = 3 R_\odot$ and the distance of the knot A1 from the star, r , equal to 100 AU (i.e., 0.2, see BWA11). We take $T_{\text{eff}} = 4000 \text{ K}$ for the stellar temperature and $6000 \text{ K} \leq T_{\text{eff}} \leq 12,000 \text{ K}$ for the hot spot temperature, following the model of Calvet & Gullbring (1998). The hot spot area has been taken between 10% and 30% of the stellar surface.

As shown by Lucy (1995), a powerful way to evaluate the relevance of photo-excitation is to compute the so-called excitation parameter (U_{ex}), which is defined as the ratio between all the radiative and collisional excitation rates involving two given levels. From U_{ex} , the “second critical electron density” can be also derived, $n_e^* = U_{\text{ex}} n_e$, such that for $n_e^* \gg n_e$, fluorescent excitation is predominant with respect to collisional excitation. Assuming a stellar field and that $n_e = 2 \times 10^4 \text{ cm}^{-3}$ (Section 3.1.1), we get $n_e^* \lesssim 10^2 \text{ cm}^{-3}$ (or $U_{\text{ex}} < 5 \times 10^{-3}$) for all the levels, indicating that fluorescence excitation is negligible in this case. The importance of the hot-spot field was tested by varying both T_{eff} and W in the ranges given above, obtaining n_e^* up to 10^5 cm^{-3} . Thus, in principle, the presence of a hot-spot could have a role in fluorescence excitation. However, the comparison of the predicted intensity ratios with those observed in the ESO-H α 574 spectrum, indicates a marginal compatibility only for the lowest values of T_{eff} and W (i.e., $T_{\text{eff}} \leq 8000 \text{ K}$ and hot-spot area not exceeding 10% of the stellar surface). Hence, even if a hot-spot may exist, certainly it is not the main cause of the observed emission. As a note, and with reference to Section 3.1.1. and Table 3, we also report that none of the line ratios systematically underestimated by the collisional model can be reproduced even if fluorescence excitation is considered.

Finally, in the Par-Lup 3-4 case, the distance between the central source and the jet is not well defined as in the ESO-H α 574 case. Taking different values of W , we estimate that the photo-excitation contribution, and in particular that due to the hot spot field, can be relevant for distances closer than 5–10 AU from the central source.

4. DISCUSSION

4.1. Comparison with Shock Models

Once we derived the physical conditions, the origin of the iron emission in the two jets was investigated in the framework of shock models. Figure 13, adapted from Figure 1 of Hartigan et al. (1994), shows the variation of the ionization fraction, electron density, and temperature with the distance behind the shock front for a low velocity (35 km s^{-1}) and an intermediate velocity (70 km s^{-1}) shock, in the approximation of a slab geometry and for assumed values of the pre-shock density and magnetic field. For each combination of these parameters, we computed the intensity of the most prominent iron lines and then derived their expected intensity variation along the overall post-shock region. In particular we show, in the left panels, the peak-normalized intensity profiles of ultra-violet, optical, near-infrared $[\text{Fe II}]$ lines (those coming from levels $a^4\text{G}$, $a^4\text{P}$, and $a^4\text{D}$), and in the middle panels the profiles of $[\text{Fe III}]$ lines coming from level $a^3\text{F}$. Notably, lines at different wavelengths peak at different distances from the shock front, in the dimensional scale of $\sim 10^{13}$ – 10^{14} cm . At the distance of our objects, these scales

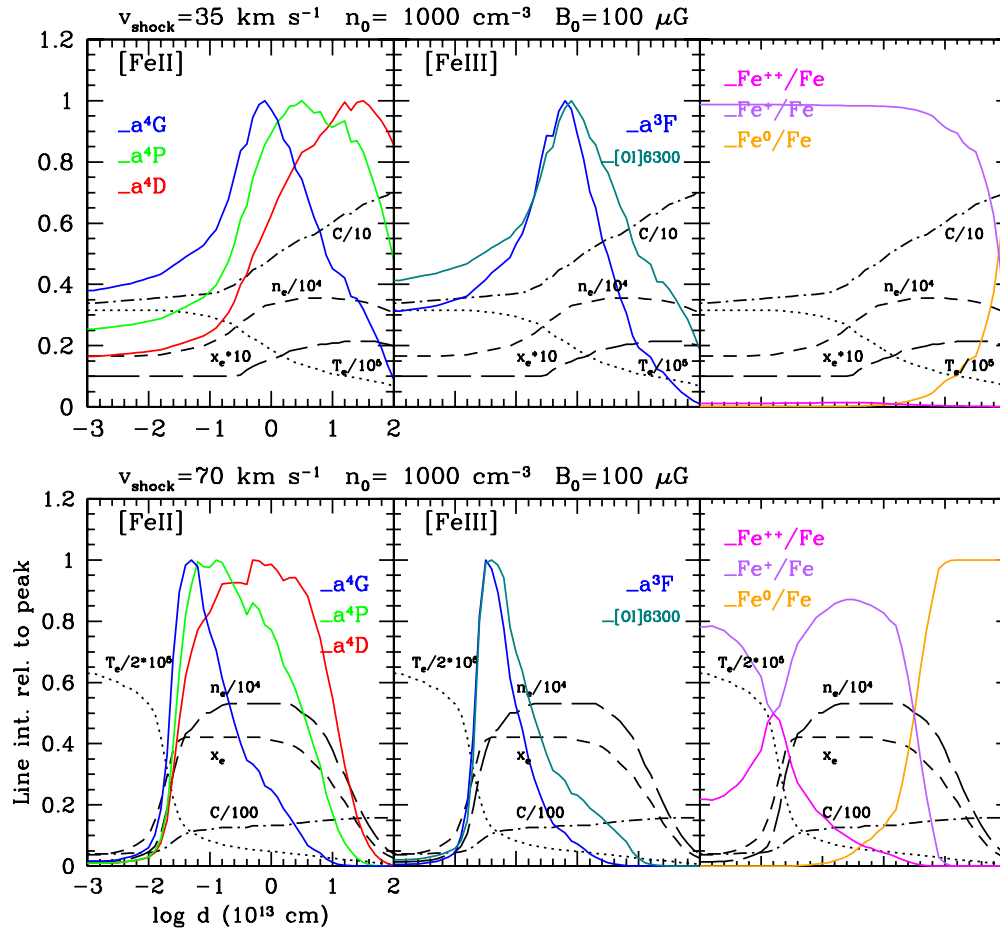


Figure 13. Post-shock intensities relative to peak values versus distance from the shock front, adapted from Figure 1 of Hartigan et al. (1994). [Fe II] and [Fe III] lines (left and middle panels, respectively) are shown for two shock velocities (35 km s^{-1} , upper panel, and 70 km s^{-1} , lower panel). For [Fe II] lines, the peak-normalized intensity profile of ultra-violet (blue), optical (green), and near-infrared (red) lines is shown. Temperature (in K, divided by 10^5 for $v_{\text{shock}} = 35 \text{ km s}^{-1}$, and 2×10^5 for $v_{\text{shock}} = 70 \text{ km s}^{-1}$), electron density (in cm^{-3} , divided by 10^4), fractional ionization (multiplied by 10 for $v_{\text{shock}} = 35 \text{ km s}^{-1}$, and by 100 for $v_{\text{shock}} = 70 \text{ km s}^{-1}$), and compression factor ($C = n_{\text{post-shock}}/n_{\text{pre-shock}}$, divided by 100 for $v_{\text{shock}} = 70 \text{ km s}^{-1}$ and by 10 for $v_{\text{shock}} = 35 \text{ km s}^{-1}$) are plotted with dotted, short-dashed, long-dashed, and dot-short-dashed curves, respectively. The assumed pre-shock gas conditions in terms of density and magnetic field strength are also reported. In addition, the middle panels show the peak-normalized intensity profile of the [O I] 6300 Å line. The right panels give the relative fraction of Fe^0 , Fe^+ , and Fe^{++} with respect to the total Fe abundance along the shock profile.

(A color version of this figure is available in the online journal.)

Table 4
Fitted Physical Parameters

	ESO-H α 574	Par-Lup 3-4
Temperature (10^4 K)	0.8–1.4	1.1–2.0
Electron density (10^4 cm^{-3})	0.8–63.0 ^a	1.8–17.7
Ionization fraction	0.65–0.85	<0.4
Gas phase iron (%)	50–60	27–33

Note. ^a The upper value is derived from the fit of [Fe II] ultra-violet lines.

correspond to hundredths of arcsec, which are not resolved at our spatial resolution, and therefore the excitation model of Fe^+ gives only average quantities.

It is also important to notice that the physical parameters derived in ESO-H α 574 and Par-Lup 3-4 cannot be directly compared with those depicted in Figure 13, which strongly depend on the assumed conditions of pre-shock density of the gas, magnetic field strength, and shock velocity. Nevertheless, a trend between post- and pre-shock parameters can be evidenced. We computed (see Table 5) the average $\langle T_e \rangle$, $\langle x_e \rangle$, $\langle n_e \rangle$, and the compression factor $C = n_{\text{post-shock}}/n_{\text{pre-shock}}$,

weighted by the intensity profiles of the various (groups of) lines depicted in Figure 13. By examining the data of Table 5, a number of conclusions can be drawn: (1) For a given shock velocity, lines at decreasing wavelengths trace progressively higher temperatures. Ionization fraction and electron density slightly increase with decreasing wavelength in the model with $v_{\text{shock}} = 70 \text{ km s}^{-1}$, while they remain fairly constant and significantly lower if $v_{\text{shock}} = 35 \text{ km s}^{-1}$. (2) The average parameters probed by the mean of all [Fe II] lines (fourth line of Table 5) indicate that increasing shock velocities correspond to decreasing temperatures and to increasing ionization fraction, electron density, and compression factor. This points toward a higher shock-velocity in ESO-H α 574, where temperature is lower and electron density and ionization fraction are higher than in Par-Lup 3-4 (see Table 4). Moreover, in the intermediate-velocity shock model, the [Fe III] lines trace more specifically the portion of the post-shock region extending up to $\sim 10^{13} \text{ cm}$ behind the shock front, where the electron density reaches its maximum value. This region should therefore correspond to that traced by the observed [Fe III] line ratios.

We also note that the above scenario is consistent with the abundance ratios of the Fe^0 , Fe^+ , and Fe^{++} depicted in the right

Table 5
Intensity-weighted Parameters in the Shock Cooling Region (Computed from the Models of Figure 13)

Lines	35 km s ⁻¹				70 km s ⁻¹			
	$\langle T_e \rangle$ (K)	$\langle x_e \rangle$...	$\langle n_e \rangle$ (cm ⁻³)	$\langle C \rangle$...	$\langle T_e \rangle$ (K)	$\langle x_e \rangle$...	$\langle n_e \rangle$ (cm ⁻³)	$\langle C \rangle$...
[Fe II] a ⁴ D	8580	0.032	207	7	5690	0.26	3610	15
[Fe II] a ⁴ P	9000	0.033	207	6	7220	0.32	4380	14
[Fe II] a ⁴ G	9760	0.034	205	6	8870	0.36	4810	14
[Fe II] all lines	9110	0.033	206	6	7260	0.31	4270	14
[Fe III] a ³ F	11900	0.034	197	6	14100	0.41	5020	13
[O I] ^a	9090	0.033	9180	0.364

Note. ^a Taken from Bacciotti & Eisloffel (1999).

panels of Figure 13. Indeed, whereas for a low-velocity shock the bulk of iron is singly ionized, for an intermediate velocity shock the ratio $\text{Fe}^+/\text{Fe}^{++} \sim 8$ (at distances of the order of 10^{13} cm), again consistent with the detection of Fe^{++} only in ESO-H α 574.

Finally, we again remark that although the above analysis allows us to interpret the observations in a consistent framework of shocked origin, the pre-shock parameters of the two models taken as a reference are not consistent with the derived post-shock parameters. For example, for the measured $\langle n_e \rangle$ and the compression factors of Table 5, the pre-shock density would be $\langle n_0 \rangle \sim 7 \times 10^3 \text{ cm}^{-3}$ and $\sim 6 \times 10^4 \text{ cm}^{-3}$ for ESO-H α 574 and Par Lup 3–4, respectively, which are higher than the n_0 values at which the two models of Hartigan et al. (1994) are computed.

4.2. Gas-phase Fe Abundance

The gas-phase Fe abundance $x(\text{Fe})$ is an indirect measure of the presence of dust inside the jet. In general, jet launching models predict that the jet is dust-free as dust is completely destroyed in the launching region by the stellar radiation. Conversely, if the jet originates from a disk region extending beyond the dust evaporation radius, it could eventually transport some dust. This, in turn, could be then partially destroyed by the shock because of vaporization and sputtering of energetic particles (e.g., Seab 1987; Jones 2000; Guillet et al. 2009). The degree of iron depletion is therefore also a function of the shock efficiency. Previous studies of $x(\text{Fe})$ in shock environments have given sparse results, from values close to solar abundance (e.g., Beck-Winchatz et al. 1996), up to intermediate (Nisini et al. 2002; Podio et al. 2006, 2009) and very high depletion factors (Mouri & Taniguchi 2000; Nisini et al. 2005). A powerful way to estimate the percentage of gas-phase iron (δ_{Fe}), relies on intensity ratios involving lines of non-refractory species emitted in similar excitation conditions, for example the $[\text{Fe II}] 1.25 \mu\text{m}/[\text{P II}] 1.18 \mu\text{m}$, as suggested by Oliva et al. (2001). Because phosphorous lines are not detected in our spectra, we investigate the possibility of using ratios involving [O I] lines. To this aim, we solved the equations of ionization equilibrium for the first three ionic stages of oxygen, together with the statistical equilibrium for the first five levels of O^0 . The radiative coefficients are taken from the NIST database,¹⁰ while the rates for collisions with electrons are from Bhatia & Kastner (1995). As a result, we get the percentage of neutral oxygen and the peak-normalized intensity profile along the post-shock region. In particular, that of [O I] 6300 Å shown in the middle panels of Figure 13, well resembles that of [Fe II] ultra-violet

lines. Therefore, we conclude that [Fe II] ultra-violet lines and [O I] 6300 Å trace the same shock region and are therefore suited to measure δ_{Fe} inside the shock. This is also roughly confirmed by the average parameters traced by the [O I] optical lines reported in Table 5 and taken from Bacciotti & Eisloffel (1999). Note also that other tracers commonly used to derive δ_{Fe} , such as [S II] 6740 Å, are not as powerful as [O I] 6300 Å because their shock profile does not resemble that of any iron line (see, e.g., Figure 3 of Bacciotti & Eisloffel 1999). The same problem arises if the [O I] 6300 Å is compared with the [Fe II] near-infrared lines (see Figure 13).

To derive δ_{Fe} , we thus selected several ratios [O I] 6300 Å¹¹ over bright ultra-violet [Fe II] lines, whose observed values are compared with those expected for the $\langle T_e \rangle$, $\langle n_e \rangle$, and $\langle x_e \rangle$ determinations derived from the iron analysis. By assuming the solar iron and oxygen abundances with respect to hydrogen of 3.16×10^{-5} and 6.76×10^{-4} (Grevesse & Sauval 1998), we estimate $\delta_{\text{Fe}} = 0.55 \pm 0.05$ and $\delta_{\text{Fe}} = 0.30 \pm 0.03$ for ESO-H α 574 and Par-Lup 3–4, respectively. This result is in agreement with the shock interpretation given in the previous section. The higher efficiency in destroying the dust in the shock in ESO-H α 574 is due to its higher velocity, as expected from models of dissociative shocks (Guillet et al. 2009). In this respect, further observational evidence is provided by the detection in ESO-H α 574 of bright lines from other refractory species, such as Ca and Ni, which, on the contrary, are barely detected in Par-Lup 3–4 (BWA11, WBA13). Finally, we note that the derived values of δ_{Fe} belong to the group of “intermediate” depletion values, where the shock has not a sufficient strength to completely destroy dust. The presence of dust inside the shock is in turn an indication that the jet launching region is larger than the dust sublimation zone.

4.3. Comparison with the Diagnostics of Other Atomic Species

Together with iron lines, the spectra of ESO-H α 574 and Par-Lup 3–4 are rich in other atomic emission lines (BWA11; WBA13), some of which are commonly used to diagnose the physical conditions of the emitting gas. In this section we intend to compare the parameters derived from iron lines with those traced by ratios of lines of oxygen, nitrogen, and sulfur. To derive the theoretical values of such ratios we have implemented simple NLTE codes for the lowest five fine structure levels of each species. The radiative coefficients are taken from the NIST database, while the electronic collision coefficients are taken from Pradhan (1976; [O II]), Pequignot & Aldrovandi (1976; [N I]), Mendoza (1983; [N II]), and Hollenbach & McKee (1989;

¹⁰ Available at <http://www.nist.gov/pml/data/asd.cfm>.

¹¹ The flux of [O I] 6300 Å is $(116.0 \pm 0.2) 10^{-17} \text{ erg s}^{-1} \text{ cm}^{-2}$ in ESO-H α 574 and $(248.3 \pm 0.3) 10^{-17} \text{ erg s}^{-1} \text{ cm}^{-2}$ in Par-Lup 3–4.

Table 6
Diagnostics of Other Atomic Lines

Ratio	ESO-H α 574		Par-Lup 3-4	
	Obs. Ratio	T_e (K)	Obs. Ratio	T_e (K)
[O I](6300+6363)/5577	26.0	11000	28.4	9000
[N II](6548+6583)/5755	28.5	12000	>15	<20000
[S II](6716+6731)/(4076+4069)	2.8	12000	0.7	>20000
	Obs. Ratio	n_e (cm $^{-3}$)	Obs. Ratio	n_e (cm $^{-3}$)
[O II](3726+3729)/(7319+7330)	1.4	2×10^5	0.4	8×10^5
[N I](5198+5200)/(10398+10407)	2.4	1×10^4	0.1	$>10^5$
[S II]6716/6731	0.6	5×10^3	0.5	10^4

[S II]). The main results of this analysis, which are summarized in Table 6, are as follows. (1) on average the temperature probed in ESO-H α 574 is in agreement with that probed with iron lines. In Par-Lup 3-4 the derived temperatures give sparse results, with T_e ([O I]) lower than T_e ([Fe II]) and with T_e ([S II]) not consistent with T_e ([N II]); (2) ratios of different species probe different electron densities, with n_e ([O II]) > n_e ([N I]) > n_e ([S II]). This result can be explained by comparing the fitted values with the critical densities of the involved lines, which, at $T_e = 10,000$ K are of $\sim 10^8$ cm $^{-3}$, $\sim 10^6$ cm $^{-3}$, and $\sim 10^4$ cm $^{-3}$ for [O II], [N I] and [S II] lines, respectively. While the densities traced with the [S II] ratio are close to the critical value, and therefore not completely reliable, this is not the case for the density indicated by the [O II] flux ratio. In ESO-H α 574 this density is the same as that inferred from the [Fe III] and [Fe II] ultra-violet lines, thus again supporting the result of a density gradient inside the jet. Notably, the [O II] line ratio indicates that in Par-Lup 3-4 the density is higher than in ESO-H α 574, in agreement with that found with the [Fe II] VIS and NIR lines.

In conclusion, care should be taken to compare physical conditions derived from different atomic species and lines, due to their different sensitivity to variations of physical parameters behind the shock front. In this respect, the rich iron spectrum from UV to NIR, with lines sensitive to a large range of excitation conditions, is particularly suited to obtain a more complete view of the post-shock cooling region.

5. SUMMARY

We have analyzed the 3000–25000 Å, X-shooter spectra, of two jets driven by low-luminosity pre-main sequence stars, ESO-H α 574 and Par-Lup 3-4, with the aim of investigating the diagnostic capabilities of the iron lines. Our analysis and main results can be summarized as follows.

1. The spectra of the two objects are both rich in iron emission. More than 70 lines are detected in ESO-H α 574 (knot A1, up to 2'' from the source), while around 35 lines are detected in the Par-Lup 3-4 jet (integrated up to 1'' from the source). The spectra show substantially different features. Whereas in the Par-Lup 3-4 jet only [Fe II] lines are detected, the spectrum of ESO-H α 574 shows both [Fe II] and [Fe III] emission. The [Fe II] lines are detected over the whole spectral range, coming from levels with energy up to more than 30,000 cm $^{-1}$. While in ESO-H α 574 the low-excitation, near-infrared lines are stronger than the high-excitation, ultra-violet lines, the opposite occurs in Par-Lup 3-4.

2. Both [Fe II] and [Fe III] line ratios are interpreted through NLTE models. These allow us to derive both the gas parameters (electron density and temperature) along with the visual extinction. The [Fe II] line fit indicates that the jet driven by ESO-H α 574 is, on average, colder ($T_e \sim 9000$ K) and less dense ($n_e \sim 2 \times 10^4$ cm $^{-3}$) than the Par-Lup 3-4 jet ($T_e \sim 13,000$ K, $n_e \sim 6 \times 10^4$ cm $^{-3}$). A more compact component ($n_e \sim 2 \times 10^5$ cm $^{-3}$) inside the jet is revealed in ESO-H α 574 if the ultra-violet lines are fitted separately from the optical and near-infrared lines. This component, whose temperature is not well constrained, is likely the same responsible for the [Fe III] line emission. The extinction appears to be negligible in both jets.
3. The contribution of fluorescence excitation due to photons emitted from the central star was investigated. In ESO-H α 574 this effect is negligible, while it can have a role in Par-Lup 3-4 up to distances less than 10 AU from the central star.
4. A ionization equilibrium code was applied to derive the fractional ionization (x_e) inside the two jets. We get $x_e \sim 0.7$ in ESO-H α 574 and $x_e \lesssim 0.4$ in Par-Lup 3-4. In particular the value detected in ESO-H α 574 is remarkably high, as expected in high-velocity shocks.
5. The observational differences evidenced in the iron spectra of the two jets have been qualitatively interpreted in the framework of shock models. The physical parameters derived from the excitation analysis are consistent with shocks with different velocities, with the shock of ESO-H α 574 being significantly faster than that of Par-Lup 3-4. Plots of post-shock [Fe II] line intensities versus distance from the shock front indicate that lines at different wavelengths trace different post-shock regions. In particular [Fe II] ultra-violet and [Fe III] lines are only emitted close to the shock front (within a distance of $\sim 10^{13}$ cm), where the post-shock density reaches its maximum value.
6. The shock strength of the jets is probed by measuring the gas-phase iron abundance (δ_{Fe}). This was derived from the ratios of fluxes of ultra-violet [Fe II] lines with that of [O I] 6300 Å. Under the assumption of solar Fe and O abundances, we derive $\delta_{Fe} \sim 0.55$ and 0.30 in ESO-H α 574 and Par-Lup, respectively. This evidence is in agreement with the higher shock-velocity of ESO-H α 574, which in turn corresponds in a higher kinetic energy able to partially destroy the dust particles.
7. The gas diagnostic derived from iron lines was compared with that obtained from bright lines of other atomic species detected in the X-shooter spectra. Although the average trend of temperature and density is the same (with

ESO-H α 574 colder than Par-Lup 3-4), the derived values are in general not consistent with each-other. We ascribe this behavior to the low number of the used lines able to cover a limited parameter range that depends on the specific line excitation energies and critical densities. Conversely, thanks both to the very rich spectrum of iron and to the wide spectral range covered with X-shooter, the analysis of iron lines allows us to get a very comprehensive and consistent view of the gas physics in the post-shock region.

We are grateful to Manuel Bautista and to an anonymous referee for their suggestions and constructive discussions. T.G. and J.M.A. thank also G. Attusino. The ESO staff is acknowledged for their support with the observations and the X-shooter pipeline.

REFERENCES

- Alcalá, J. M., Natta, A., Manara, C. F., et al. 2013, A&A, in press (arXiv:1310.2069)
- Alcalá, J. M., Stelzer, B., Covino, E., et al. 2011, *AN*, 332, 242
- Arnaud, M., & Raymond, J. 1992, *ApJ*, 398, 394
- Bacciotti, F., & Eislöffel, J. 1999, A&A, 342, 717
- Bacciotti, F., Whelan, E. T., Alcalá, J. M., et al. 2011, *ApJ*, 737, 26 (BWA11)
- Bautista, M. A., Fivet, V., Quinet, P., et al. 2013, *ApJ*, 770, 15
- Bautista, M. A., & Kallman, T. R. 2001, *ApJS*, 134, 139
- Bautista, M. A., Peng, J., & Pradhan, A. K. 1996, *ApJ*, 460, 372
- Bautista, M. A., & Pradhan, A. K. 1998, *ApJ*, 492, 650
- Beck-Winchatz, B., Bohm, K.-H., & Noriega-Crespo, A. 1996, *AJ*, 111, 346
- Bhatia, A. K., & Kastner, S. O. 1995, *ApJ*, 96, 325
- Calvet, N., & Gullbring, E. 1998, *ApJ*, 509, 802
- Comerón, F., Fernández, M., Baraffe, I., et al. 2003, *A&A*, 406, 1001
- Comerón, F., & Reipurth, B. 2006, *A&A*, 458, 21
- Draine, B. T. 2003, *ARA&A*, 41, 241
- Fernández, M., & Comerón, F. 2005, *A&A*, 440, 1119
- Ferreira, J. 1997, A&A, 319, 340
- Giannini, T., Calzoletti, L., Nisini, B., et al. 2008, *A&A*, 481, 123
- Grevesse, N., & Sauval, A. J. 1998, *SSRv*, 85, 161
- Guillet, V., Jones, A. P., & Pineau Des Forêts, G. 2009, *A&A*, 497, 145
- Hartigan, P., & Morse, J. 2007, *ApJ*, 660, 426
- Hartigan, P., Morse, J. A., & Raymond, J. 1994, *ApJ*, 436, 125
- Hollenbach, D., & McKee, C. F. 1989, *ApJ*, 342, 306
- Huélamo, N., Bouy, H., Pinte, C., et al. 2010, *A&A*, 523, A42
- Jones, A. P. 2000, *JGR*, 105, 10257
- Kingdon, J. B., & Ferland, G. J. 1996, *ApJS*, 106, 205
- Lucy, L. B. 1995, A&A, 294, 555
- Luhman, K. L. 2007, *ApJS*, 173, 104
- Mendoza, C. 1983, in IAU Symp. 103, Planetary Nebulae, ed. D. R. Flower (Dordrecht: Reidel), 143
- Merín, B., Jørgensen, J., Spezzi, L., et al. 2008, *ApJS*, 177, 551
- Mouri, H., & Taniguchi, Y. 2000, *ApJL*, 534, L63
- Nisini, B., Antonucci, S., Giannini, T., & Lorenzetti, D. 2005, *A&A*, 429, 543
- Nisini, B., Caratti o Garatti, A., Giannini, T., & Lorenzetti, D. 2002, *A&A*, 393, 1035
- Oliva, E., Marconi, A., Maiolino, R., et al. 2001, *A&A*, 369, L5
- Pequignot, D., & Aldrovandi, S. M. V. 1976, A&A, 50, 141
- Podio, L., Bacciotti, F., Nisini, B., et al. 2006, *A&A*, 456, 189
- Podio, L., Eislöffel, J., Melnikov, S., Hodapp, K. W., & Bacciotti, F. 2011, *A&A*, 527, A13
- Podio, L., Medves, S., Bacciotti, F., et al. 2009, *A&A*, 506, 779
- Pradhan, A. K. 1976, *MNRAS*, 177, 31
- Ray, T., Dougados, C., Bacciotti, F., Eislöffel, J., & Chrysostomou, A. 2007, in Protostars and Planets V, ed. B. Reipurth, D. Jewitt, & K. Keil (Tucson, AZ: Univ. Arizona Press), 231
- Seab, C. G. 1987, in Interstellar Processes, ed. D. I. Hollenbach & H. A. Thronson (Dordrecht: Reidel), 491
- Shu, F., Najita, J., Ostriker, E., et al. 1994, *ApJ*, 429, 781
- Whelan, E. T., Bonito, R., Antonucci, S., et al. 2013, A&A, submitted (WBA13)
- Wichmann, R., Bastian, U., Krautter, J., et al. 1998, *MNRAS*, 301, 39